AGU PUBLICATIONS

JGR

Journal of Geophysical Research: Atmospheres

RESEARCH ARTICLE

10.1002/2016JD025307

Key Points:

- The convection in the typhoon rainband contains smaller drops and higher number concentrations than the maritime type convection
- The conversion of cloud water into rainwater through cloud water accretion by raindrops dominates the heavy rainfall
- The precipitation efficiency is over 50% for the typhoon rainband

Correspondence to:
K. Zhao,
zhaokun@nju.edu.cn

Citation:
Wang, M., K. Zhao, M. Xue, G. Zhang, S. Liu, L. Wen, and G. Chen (2016), Precipitation microphysics characteristics of a Typhoon Matmo (2014) rainband after landfall over eastern China based on polarimetric radar observations, *J. Geophys. Res. Atmos.*, *121*, 12,415–12,433, doi:10.1002/2016JD025307.

Received 2 MAY 2016
Accepted 30 SEP 2016
Accepted article online 6 OCT 2016
Published online 28 OCT 2016

Precipitation microphysics characteristics of a Typhoon Matmo (2014) rainband after landfall over eastern China based on polarimetric radar observations

Mingjun Wang[1], Kun Zhao[1], Ming Xue[1,2,3], Guifu Zhang[1,3], Su Liu[1], Long Wen[1], and Gang Chen[1]

[1]Key Laboratory of Mesoscale Severe Weather/MOE and School of Atmospheric Sciences, Nanjing University, Nanjing, China, [2]Center for Analysis and Prediction of Storms, University of Oklahoma, Norman, Oklahoma, USA, [3]School of Meteorology, University of Oklahoma, Norman, Oklahoma, USA

Abstract The evolution of microphysical characteristics of a rainband in Typhoon Matmo (2014) over eastern China, through its onset, developing, mature, and dissipating stages, is documented using observations from an S band polarimetric Doppler radar and a two-dimensional video disdrometer (2DVD). The drop size distributions observed by the 2DVD and retrieved from the polarimetric radar measurements indicate that the convection in the rainband generally contains smaller drops and higher number concentrations than the typical maritime type convection described in Bringi et al. (2003). The average mass-weighted mean diameter (D_m) of convective precipitation in the rainband is about 1.41 mm, and the average logarithmic normalized intercept (N_w) is 4.67 $\log_{10}\,\mathrm{mm}^{-1}\,\mathrm{m}^{-3}$. To further investigate the dominant microphysical processes, the evolution of the vertical structures of polarimetric variables is examined. Results show that complex ice processes are involved above the freezing level, while it is most likely that the accretion and/or coalescence processes dominate below the freezing level throughout the rainband life cycle. A combined examination of the polarimetric measurements and profiles of estimated vertical liquid and ice water contents indicates that the conversion of cloud water into rainwater through cloud water accretion by raindrops plays a dominant role in producing heavy rainfall. The high estimated precipitation efficiency of 50% also suggests that cloud water accretion is the dominant mechanism for producing heavy rainfall. This study represents the first time that radar and 2DVD observations are used together to characterize the microphysical characteristics and precipitation efficiency for typhoon rainbands in China.

1. Introduction

Landfalling tropical cyclones (TCs) usually bring heavy rainfall to coastal regions and often result in inland flooding and mudslides that can produce disastrous impacts on human lives and properties. Improving quantitative precipitation estimate (QPE) and forecast (QPF) for TCs is crucial for disaster mitigation; however, QPE and QPF skills still lag behind track or even intensity forecasts [*Duan and Liu*, 2010]. Key factors that may help improve TC precipitation forecast include improved understanding of microphysical processes within TC eyewall and rainbands (e.g., drop size distribution (DSD)) that contribute to the development of heavy rainfall [*Morrison et al.*, 2009; *Duan and Liu*, 2010].

Earlier studies on the precipitation characteristics of landfalling TCs, including the radar reflectivity Z and rain rate R (Z-R) relationships, were often based on observations from weather radars and/or surface-based disdrometers [e.g., *Wilson and Pollock*, 1974; *Ulbrich and Lee*, 2002; *Tokay et al.*, 2008; *Chen et al.*, 2012]. Recent studies have used polarimetric radar data (PRD) to investigate the microphysical characteristics of TCs [e.g., *May et al.*, 2008; *Chang et al.*, 2009; *Brown et al.*, 2016].

Studies based on disdrometer observations [*Tokay et al.*, 2008; *Chang et al.*, 2009; *Chen et al.*, 2012] have found that TC convective precipitation possesses a high concentration of small- and/or medium-sized drops; thus, the precipitation is usually classified as the maritime convective type [*Bringi et al.*, 2003]. These studies also found different DSD characteristics within TCs in the Atlantic and Pacific basins. DSDs collected from 3 years of Atlantic TCs in the coastal regions of the U.S. possessed high concentrations of small- and/or medium-sized drops and very low concentrations of large drops, with a mean mass-weighted diameter

(D_m) of 1.67 ± 0.3 mm and a disdrometer-calculated reflectivity of 40 dB*Z* [*Tokay et al*., 2008]. For 13 western Pacific typhoons that made landfall in Taiwan, *Chang et al*. [2009] found that precipitation in typhoons possessed a D_m of ~2 mm and a mean logarithmic normalized intercept parameter (N_w) of ~3.8 $\log_{10}$ mm^{-1} m^{-3}, which fall between the diameters and intercept parameter ranges of maritime and continental convective rainfall [*Bringi et al*., 2003, Figure 11]. The DSDs retrieved from a C band polarimetric radar measurements for precipitation over the ocean showed more of the maritime type [*Chang et al*., 2009]. The DSDs collected by a laser-optical Particle Size Velocity (PARSIVEL) disdrometer manufactured by OTT Germany from Typhoon Morakot (2009) during its landfall in eastern China showed a D_m of ~1.54 mm in the convective region [*Chen et al*., 2012], which is smaller than those in Atlantic and western Pacific TCs.

The differences in observed DSDs are directly related to complex microphysical processes [e.g., *Bringi et al*., 2003; *Rosenfeld and Ulbrich*, 2003]. In addition, the spatial and temporal evolution of DSDs can be used to identify microphysical processes of precipitation, such as warm rain processes directly corresponding to the variances in DSDs [*Rosenfeld and Ulbrich*, 2003]. These aforereferenced studies primarily used disdrometer to derive the DSD information. Note that disdrometer data are only point measurements at the surface, while polarimetric radars can provide three-dimensional (3-D) information related to the size, shape, and orientation of the hydrometeors covering large domains [*Bringi and Chandrasekar*, 2001; *Doviak and Zrnić*, 2006]. The polarimetric radar data (PRD), given their high temporal resolution, can also provide information regarding the evolution of DSD [*Zhang et al*., 2001].

Polarimetric radar measurements depend on the number, size, shape, orientation, and the dielectric property of precipitation particles and can thus be used to infer ice and warm rain processes [*Hence and Houze*, 2011; *Andrić et al*., 2012; *Hence and Houze*, 2012; *Kumjian and Ryzhkov*, 2012; *Kumjian and Prat*, 2014]. The microphysical processes strongly affect precipitation efficiency and therefore rainfall rate at the surface [e.g., *Murata*, 2009; *Chang et al*., 2015]. To our knowledge, the time evolution and spatial distribution of DSDs and the dominant microphysical processes in TC rainbands over land using PRD have not been documented in the literature.

During the intensive observing period No. 10 (IOP10) of the Observation, Prediction and Analysis of Severe Convection of China (OPACC) project in 2014, Typhoon Matmo made landfall at 0730 UTC 23 July 2014 in Fuqing, Fujian Province, China, as a tropical storm. It moved inland, weakened, and passed over one of the intensive observation areas of OPACC in Nanjing, Jiangsu Province of China. One of the rainbands (Matmo was disorganized after making landfall. The precipitation north of the center became a wide zone where the eyewall could no longer be identified. Therefore, we decided to call this precipitation zone a rainband.) in Matmo developed to mature stage from 0800 to 1300 UTC, 24 July. The rainband weakened after 1300 UTC and dissipated at around 1500 UTC. During this period, the rainband was, for the first time in China, well captured by a trio of instruments: an S band polarimetric Doppler radar located in Lishui (Lishui Radar, marked as LSRD), Nanjing, Jiangsu Province; a Chinese Meteorology Administration (CMA) operational S band Doppler radar (Nanjing Radar, marked as NJRD); and a third-generation two-dimensional video disdrometer (2DVD) located in Nanjing (Figure 1). The LSRD and 2DVD data provide microphysical information, while dual-Doppler analyses from LSRD and NJRD data provide kinematical structure of the rainband. This study examines the evolution of DSD and the corresponding microphysical processes in Typhoon Matmo's rainband throughout its life cycle.

The rest of the paper is organized as follows. The observational data and analysis methods are described in section 2. The synoptic conditions, the structure, and evolution of the rainband are presented in section 3. Section 4 discusses the DSDs and their evolution during the rainband life cycle, while the vertical structure of rainband is examined in section 5. The dominant microphysical process and the precipitation efficiency are discussed in section 6. Finally, summary and conclusions are given in section 7.

2. Data and Methodology

2.1. Data and Their Processing

2.1.1. 2DVD Data and Processing

The 2DVD is a fast-scanning instrument with a rectangular sample area of 10 cm by 10 cm and a grid resolution of close to 0.2 mm for both the horizontal and vertical directions. The 2DVD used in this study was deployed at about 37 km northwest of LSRD at Jiangning (JN) site (see Figure 1). One minute DSDs collected by the 2DVD with drop counts over 50 are included in this analysis to minimize biases due to sampling errors.

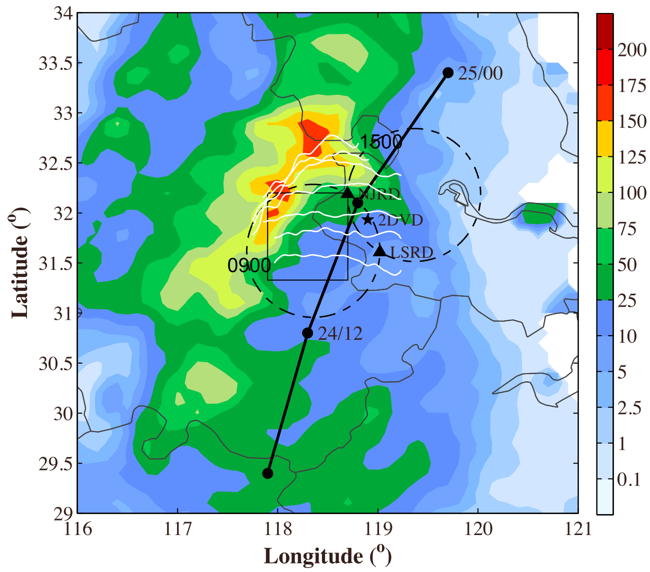

Figure 1. The 12 h accumulated precipitation (shading, mm) from 0600 UTC to 1800 UTC 24 July 2014, along with the best track (solid black line and black dots) from China Meteorological Administrator (CMA) every 6 h from 0600 UTC 24 July to 0000 UTC 25 July 2014. Triangles indicate the locations of the LSRD and NJRD radars. Star shows the location of Jiangning (JN) site operating 2DVD and sounding measurements. Black dashed circles represent the dual-Doppler synthesis lobes of LSRD and NJRD. Solid box indicates the dual-Doppler analysis area. White lines represent the rainband locations from 0900 UTC to 1500 UTC every 1 h.

The DSDs are first processed using a sorting and averaging algorithm based on the two parameters method [*Cao et al.*, 2008] to minimize the sampling error, and then the DSD parameters, such as D_m and N_w, are further calculated using the truncated moment fitting method [*Vivekanandan et al.*, 2004]. About one thousand 1 min DSD samples are obtained for Typhoon Matmo, in which are about 90 consecutive 1 min DSD samples for the particular rainband examined in this study.

For fair comparisons with previous studies, the normalized gamma DSD [*Testud et al.*, 2001; *Bringi et al.*, 2003], instead of the gamma distribution [*Ulbrich*, 1983], was used to examine the DSD characteristics. The normalized gamma distribution of DSD is expressed as the function of the normalized intercept parameter (N_w), the mass-weighted mean diameter (D_m), and the shape parameter (μ) of the gamma DSD:

$$N(D) = N_w f(\mu)\left(\frac{D}{D_m}\right)^{\mu} \exp\left[-(4+\mu)\frac{D}{D_m}\right], \quad (1)$$

where D (mm) is the equivalent diameter and $N(D)$ (m^{-3} mm^{-1}) is the number concentration of raindrops in a unit volume of air and a unit size interval. For a DSD, the nth-order moment is defined as

$$M_n = \int_0^{D_{max}} D^n N(D)\mathrm{d}D. \quad (2)$$

Then, D_m (mm) is defined as the ratio of the fourth to the third moment of the DSD:

$$D_m = \frac{M_4}{M_3}. \quad (3)$$

Also, the water content is calculated from the third moment as

$$W = \frac{\pi}{6}\rho_w M_3, \quad (4)$$

where ρ_w (1000 kg m^{-3}) is the water density. N_w (mm^{-1} m^{-3}) is then computed from W and D_m:

$$N_w = \frac{4^4}{\pi\rho_w}\left(\frac{10^3 W}{D_m^4}\right). \quad (5)$$

The detailed definition can be found in *Bringi et al.* [2003]. Generally, D_m is a measurement of the mean drop size, and N_w represents the number concentration of a DSD. Note that D_m and N_w are calculated directly from a 2DVD-measured DSD without fitting the measurements to the normalized gamma model.

2.1.2. Radar Data

The LSRD polarimetric Doppler radar has a 0.92° beam width and a 150 m range resolution and is operated in the VCP (volume coverage pattern) 11 mode consisting of 14 elevations between 0.5° and 19.5° [*Crum et al.*, 1993]. In addition to VCP 11, the LSRD also performed a few vertical pointing scans at 90° elevation in light rain for differential reflectivity (Z_{DR}) calibration purpose [*Bringi and Chandrasekar*, 2001]. The PRD used in this study include radar reflectivity factor of horizontal polarization (Z_H), differential reflectivity (Z_{DR}), and specific differential phase (K_{DP}). Note that Z_{DR} provides information about the oblateness of particles, and K_{DP} mainly depends on the liquid water content [*Bringi and Chandrasekar*, 2001]. Specifically, Z_{DR} well represents the median drop size of liquid DSD. Detailed descriptions of these variables can be found in previous articles [e.g., *Bringi and Chandrasekar*, 2001; *Kumjian*, 2013]. The NJRD Doppler radar is located at ~ 72 km northwest of LSRD and was also operated in the VCP 11 mode. The maximum unambiguous ranges of LSRD and NJRD are 150 km and 230 km, respectively.

The NJRD and LSRD Doppler velocities are first manually edited to unfold radial velocity and remove nonmeteorological echoes. The nonmeteorological echoes of LSLD are further removed when $\rho_{hv} < 0.85$ [*Giangrande and Ryzhkov*, 2008]. This ρ_{hv} threshold may remove some useful data but should not affect the statistical results in this study. A five-gate median average and a five-gate running mean are performed for Z_H and Z_{DR}, respectively, to reduce the random fluctuations [*Schuur et al.*, 2003]. The differences between LSRD-measured Z_{DR} and disdrometer-calculated Z_{DR} at the disdrometer location are within 0.2 dB, suggesting that the LSRD-measured Z_{DR} data are well corrected.

2.2. Dual-Doppler Wind Retrieval

After quality control, the radar data are interpolated onto a Cartesian grid with 1.0 km horizontal and 0.5 km vertical spacing using the NCAR REORDER software package (more information is available online at http://www.eol.ucar.edu/rsf/UserGuides/ELDORA/DataAnalysis/reorder/unixreorder.ps). The lowest grid altitude is 0.5 km. The three wind components are then retrieved using the Cartesian Editing and Display of Radar Data under Interactive Control (CEDRIC) software [*Mohr et al.*, 1986] every 8 min from 0900 UTC to 1200 UTC. The retrieved wind fields cover an 80 km × 90 km region (Figure 1) extending to 15 km in altitude. The vertical velocity was obtained using a variational integration scheme within CEDRIC, with the fraction parameter of 0.5 for both upward and downward integration.

2.3. Microphysical Analysis Methods

2.3.1. DSD Retrieval

Apart from being measured by the 2DVD at the surface, the DSDs are also retrieved from the PRD using a two-parameter constrained gamma (C-G) model proposed by *Zhang et al.* [2001]. Due to climate region dependency, the shape-slope (μ-Λ) constraining relation is derived specifically for our analyses by fitting a second-order polynomial using all the 2DVD data samples collected for Typhoon Matmo as follows:

$$\mu = -0.021\Lambda^2 + 1.075\Lambda - 2.979. \tag{6}$$

This relation is similar to that derived from TCs making landfall in Taiwan [*Chang et al.*, 2009]. Based on the refined μ-Λ relation, the C-G model for Typhoon Matmo is built, and the time series of the DSDs from 0800 to 1500 UTC are obtained. The direct comparison of the LSRD-retrieved DSD against the 2DVD-observed DSD is given in section 4.

In this study, raindrops are considered as small or large if the diameter of a raindrop is less than 1 mm or larger than 3 mm, respectively; otherwise, they are classified as medium. For maritime convective precipitation [*Bringi et al.*, 2003], a DSD with D_m less than 1.75 mm is usually characterized with a large population of small and medium drops. Since a Z_{DR} of ~1.4 dB is corresponding to a D_m of ~1.75 mm based on DSD retrieval, a Z_{DR} less than 1.4 dB can indicate the dominance of small and medium raindrops.

2.3.2. Rain and Ice Water Content Estimation

To estimate the rain and ice water contents from LSRD measurements, the horizontal polarization reflectivity (Z_H, dBZ) is first analyzed to separate water and ice using the difference reflectivity (Z_{DP}, dB) method [*Carey and Rutledge*, 2000], resulting in calculations of the relative contents of ice and water. A Z^{rain}-Z_{DP} relation used to estimate rain portion of Z_H is determined from all 2DVD observations in Typhoon Matmo and is expressed as

$$Z^{rain} = 0.851Z_{DP} + 12.5. \tag{7}$$

For rain mass only (when the fraction of rain is 1), the C-G model retrieval is applied to calculate the water content [*Zhang et al.*, 2001]. In the presence of mixed-phase precipitation (when the fraction of rain is between 0 and 1), the rain mass and ice mass are estimated using the reflectivity-water content, *Z-M*, relationships adopted from previous studies [*Carey and Rutledge*, 2000; *Cifelli et al.*, 2002; *Chang et al.*, 2015]:

$$M_w = 3.44\times10^{-3}\left(Z^{\text{rain}}\right)^{4/7} \tag{8}$$

and

$$M_i = 1000\pi\rho_i N_0^{3/7}\left(\frac{5.28\times10^{-18}Z^{\text{ice}}}{720}\right), \tag{9}$$

where M_w and M_i are the water contents of rain and ice, respectively. When only ice exists, the ice mass is estimated via (9).

2.4. Classification of Precipitation Types

To investigate the characteristics of convective and stratiform precipitation, two algorithms are adopted to separate convective and stratiform regions. For DSD analyses, a threshold of 10 mm h^{-1} rainfall rate is used to separate convective and stratiform precipitation in order to compare with previous studies [*Bringi et al.*, 2003; *Chang et al.*, 2009]. For polarimetric radar measurements, the precipitation type is identified from radar reflectivity at 2 km height using a robust separation algorithm [*Steiner et al.*, 1995] by examining the spatial uniformity and intensity. This classification is used to compute contoured frequency by altitude diagrams (CFADs) in section 5 consistent with those in previous studies [e.g., *Didlake and Houze*, 2009].

3. Environmental Conditions and Evolution of the Rainband

3.1. Environmental Conditions

Matmo was rated as a tropical storm during the analysis period with a minimum sea level pressure of 992 hPa and a maximum surface wind of 20 m s^{-1}. Matmo moved north-northeastward, steered by the southwesterly wind at the west edge of the subtropical high (Figures 1 and 2). It also carried ample water vapor where the mixing ratio of water vapor (Q_v) at 850 hPa is over 16 g kg^{-1} in the target area (white boxes in Figures 2a, 2d, and 2g).

The Jiangning (JN) sounding at 1100 UTC 24 September (Figure 3) describes the environmental thermodynamic structure around the rainband during the IOP. The dewpoint temperature profile shows a very moist environment below 400 hPa with the relative humidity exceeding 80%. At the surface, the air is almost saturated, with a relative humidity of 96%, resulting in a very low lifting condensation level at ~ 73 m. This, in conjunction with a freezing level at ~ 5.5 km, allows for a deep layer of warm clouds, which is favorable for warm rain processes. The convective available potential energy (CAPE) is moderate at ~1404 J kg^{-1} with the positive area uniformly distributed between 900 and 150 hPa, indicating that the CAPE is in favor of convection but the maximum updraft intensity is limited.

3.2. Evolution of the Rainband

The Z_H, Z_{DR}, and K_{DP} at the 0.5° elevation PPI observed by LSRD from 0900 to 1500 UTC in 2 h interval are portrayed in Figure 4. At 0900 UTC, Z_H of the typhoon rainband was generally less than 40 dB*Z* with a few embedded cells (Figure 4a). The rainband then intensified rapidly and was dominated by Z_H over 40 dB*Z* until 1300 UTC (Figures 4d and 4g). At 1500 UTC, the rainband weakened and began to move out of the range of LSRD (Figure 4j). It is noted that most of Z_{DR} values are less than 1.5 dB (Figures 4b, 4e, 4h, and 4k) even at its mature stage (1300 UTC), suggesting that the precipitation is dominated by small and medium raindrops. The K_{DP} values can be over 3°km^{-1} located at about 100 km, north-northwest of LSRD (Figure 4i), indicating the existence of high liquid water content.

To further investigate the evolution of the rainband, the time-radius Hovmöller diagram (Figure 5) is constructed with the composite reflectivity averaged along each radial between 110 and 170 km from the typhoon center. The evolution of the rainband is divided into four stages, the onset (S1, 0800–1000 UTC), developing (S2, 1000–1130 UTC), mature (S3, 1130–1300 UTC), and dissipating (S4, 1300–1500 UTC) stages. During the onset stage, the rainband consists of weak precipitation with a maximum reflectivity less than 30 dB*Z*. The rainband intensified rapidly during the developing stage, with the mean reflectivity exceeding 40 dB*Z* in the mature stage. The rainband weakened in the dissipating stage.

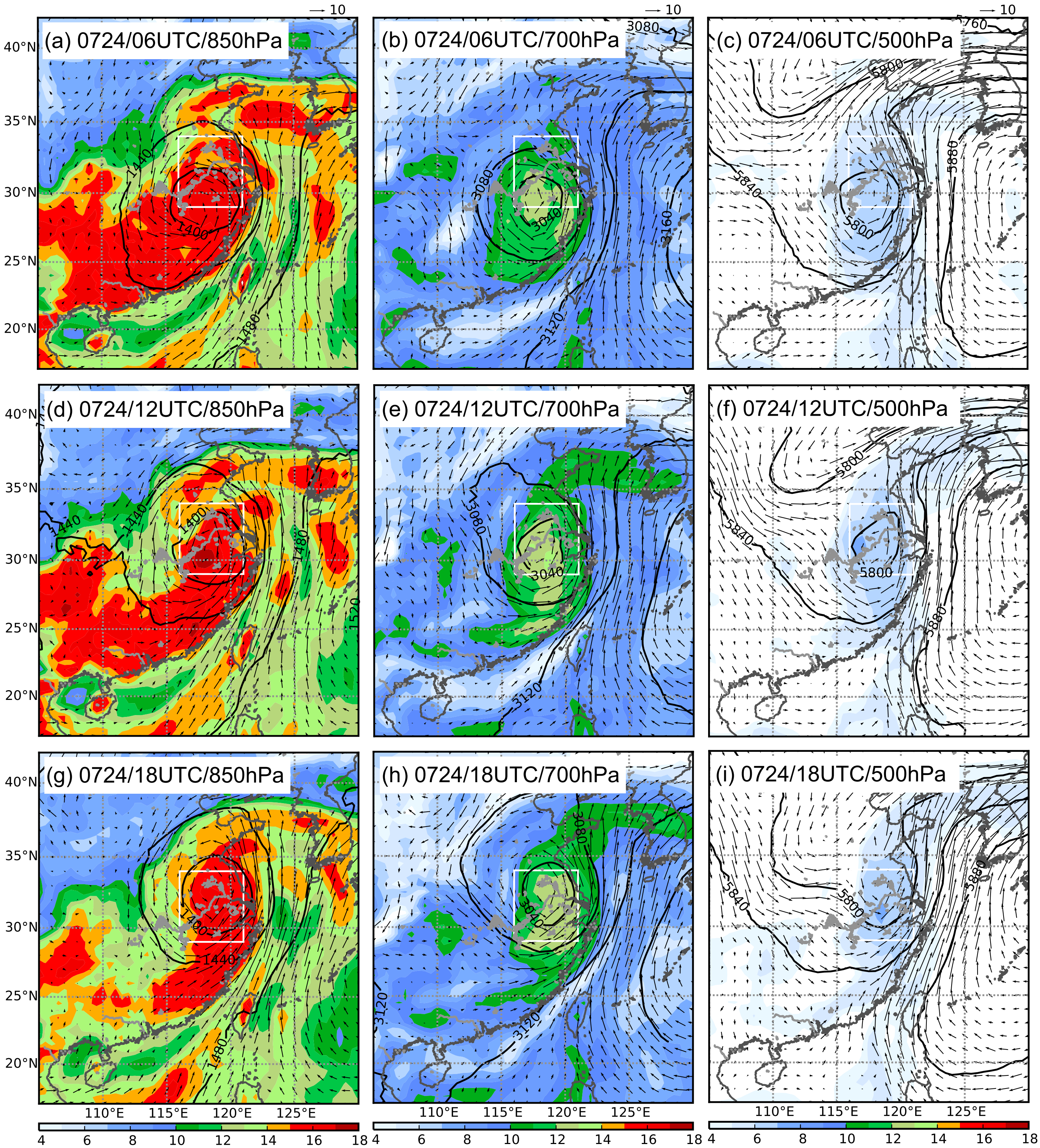

Figure 2. The mixing ratio of water vapor (g kg^{-1}), wind fields (m s^{-1}), and geopotential height (m) at 850, 700, and 500 hPa from the National Centers for Environmental Prediction's Global Forecast System analysis data at 0600–1800 UTC is shown as shaded, vectors, and contours, respectively. The reference wind vectors (10 m s^{-1}) are also shown at the top of figure.

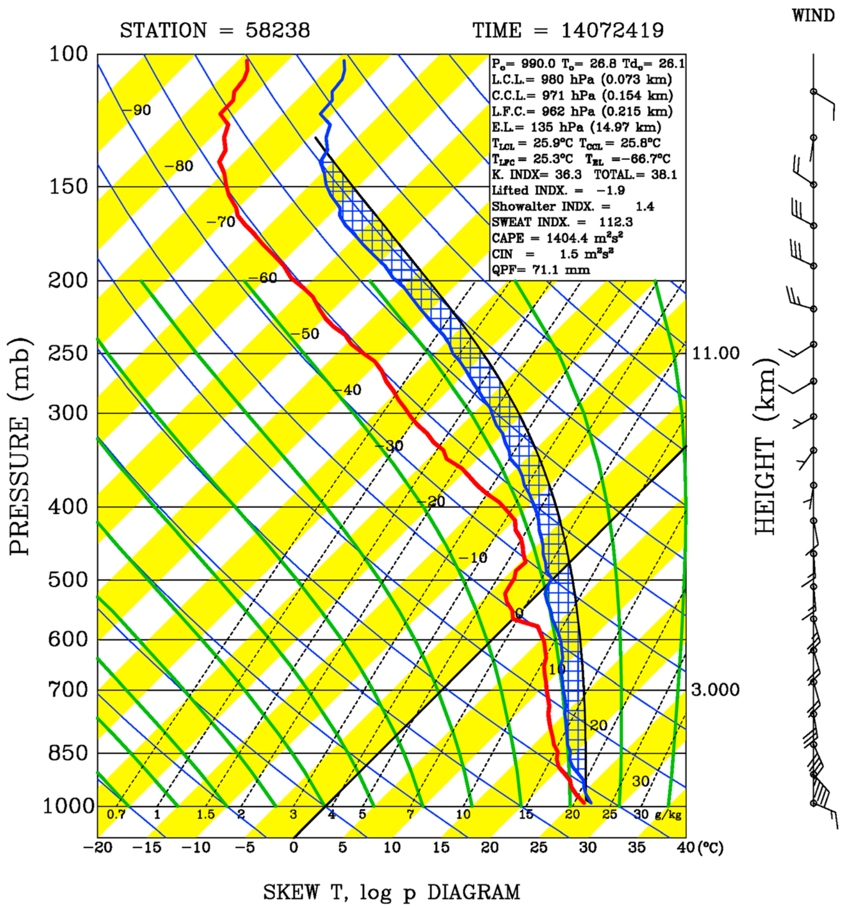

Figure 3. The skew *T*-LogP diagram and vertical wind profile of the Jiangning radiosound (star in Figure 1). The blue and red lines are temperature and dewpoint temperature profiles, respectively. The black curve is the ascending path of a surface-based parcel.

4. Evolution of the DSDs

The time series of the DSD, mass-weighted mean diameter D_m, rainfall rate, and forward-calculated reflectivity obtained from the 2DVD data at the JN site (Figure 6) only captured the DSDs within the rainband during S2 (from 1000 UTC 24 to 1130 UTC 24 July 2014) (Figure 4). The DSDs generally exhibit high concentration of small drops with the presence of very few large drops (Figure 6a). The D_m of each 1 min DSD sample varies from 0.5 to 1.7 mm, whereas the maximum diameter varies from 1 mm to over 6 mm. During this period, the heaviest 1 min rainfall rate is ~94 mm h^{-1}, and the corresponding reflectivity is about 52 dB*Z*, indicating intense convection. This extreme rainfall rate is accompanied by a DSD that has a few large raindrops and very high concentration of small- and/or medium-sized raindrops (Figure 6). In contrast, large raindrops are absent, and the number concentration, D_m, and reflectivity Z_H are much smaller when the rainfall rate is less than 10 mm h^{-1}.

To further examine the evolution of the DSDs, the DSDs are retrieved from the lowest elevation (0.5°) of LSRD-observed Z_H and Z_{DR} using the derived C-G model for Matmo in section 2.2. The frequencies of occurrence of D_m and N_w are calculated from the retrieved DSDs for four different stages and are shown in Figure 7. The rainfall rate of 10 mm h^{-1} is used as a criteria to separate the stratiform (rainfall rate less than 10 mm h^{-1}) and convective (rainfall rate greater than 10 mm h^{-1}) precipitation [*Chang et al*., 2009]. The rainfall rate increases (decreases) toward right (left) of the contour of 10 mm h^{-1}. The values of D_m and N_w calculated from the 2DVD are also plotted to verify the retrieved DSDs (Figure 7b). Results show that the values from the 2DVD are well covered by the retrieved values from LSRD, except for some small drops ($D_m < 0.8$). For convective precipitation, the mean values of D_m and N_w from 2DVD and LSRD are close to each other

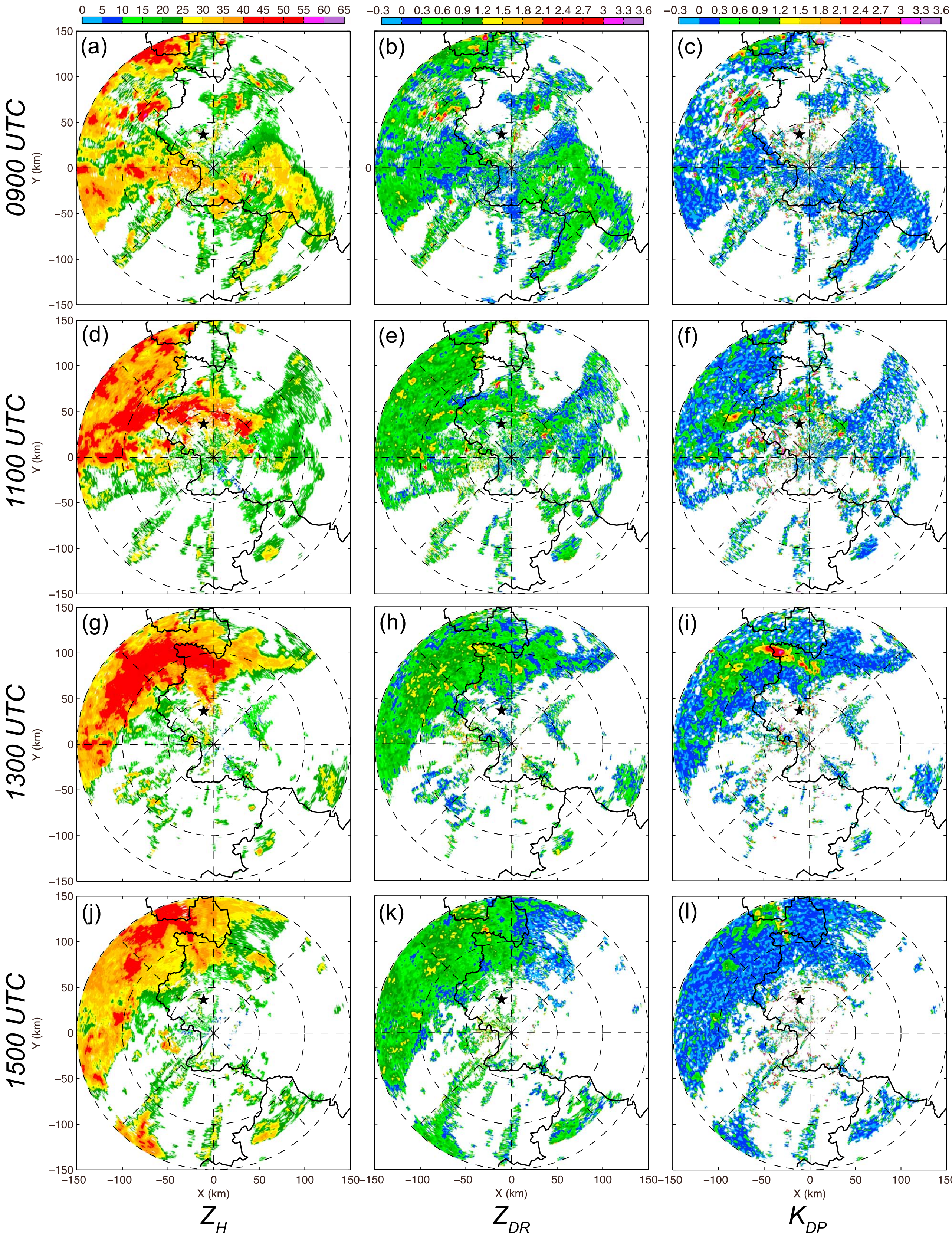

Figure 4. The (a, d g, j) reflectivity, (b, e, h, k) differential reflectivity, (c, f, i, l) and specific differential phase at 0.5° elevation observed by LSRD at 0900 UTC (first row), 1100 UTC (second row), 1300 UTC (third row), and 1500 UTC (fourth row), 24 September 2014. Stars indicate the location of 2DVD.

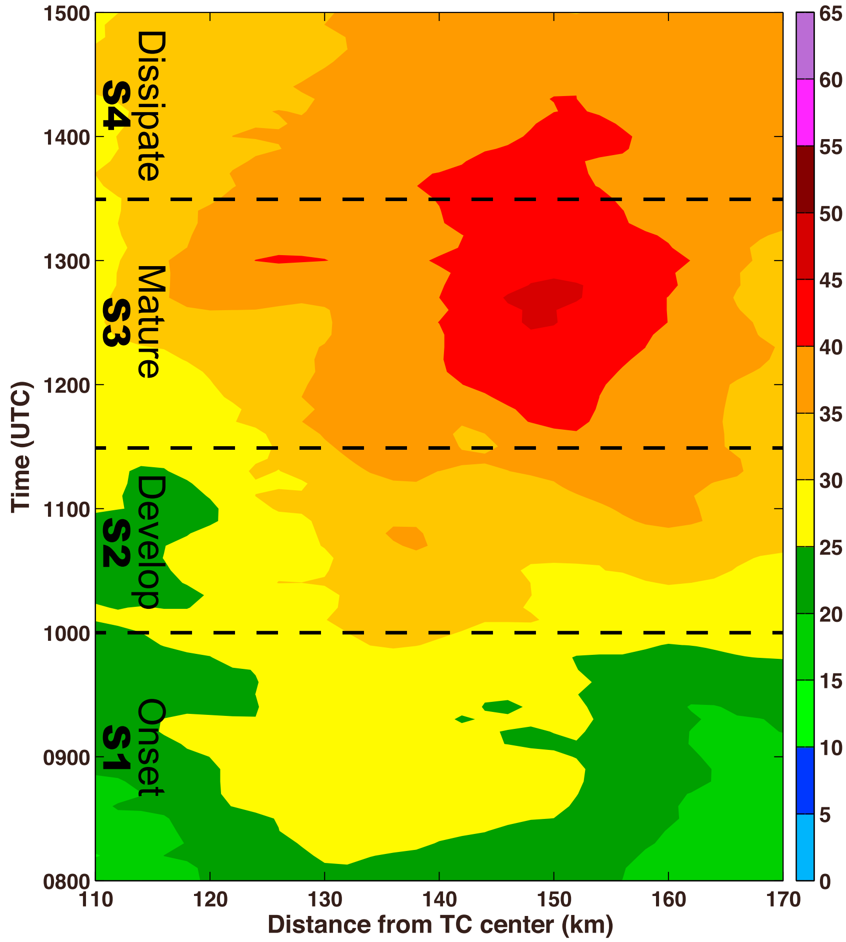

Figure 5. Time-radius Hovmöller diagrams of line-averaged (details in section 3.2) composite reflectivity of the rainband.

(Figure 7b). The mean D_m from 2DVD data is slightly smaller than that of LSRD, which can be attributed to the limited samples. Generally, the DSDs retrieved from Z_H and Z_{DR} of LSRD are consistent with those observed by 2DVD.

During S1, the distributions of D_m and N_w show a higher frequency for stratiform precipitation than convective precipitation (Figure 7a). The D_m is quite similar for stratiform and convective precipitation during S1, and the higher rainfall rate is mainly achieved through the increase of number concentration. For S2 (Figure 7b), the fraction of convective precipitation increases rapidly with a larger D_m. The D_m from stratiform precipitation does not change much, while the N_w is twice as much as that of S1, suggesting that the number concentration of raindrops has increased significantly. The D_m and rainfall rate continuously increase until the mature stage where the convective precipitation becomes dominant (Figure 7c). During S4, the stratiform precipitation is dominant again while the convective precipitation weakens (Figure 7d). The D_m of convective precipitation is similar to that during the mature stage, while N_w is reduced, implying that the generation of raindrops slows or stops during the dissipating stage.

The average values of D_m and N_w from the convective precipitation in each of the four stages are compared to those in previous studies of *Bringi et al.* [2003] and *Chang et al.* [2009]. The average D_m and N_w (black square in Figure 7) clearly show the growth of raindrop size as the rainband intensifies and the decrease of number concentration when the rainband dissipates. By comparing the values of D_m and N_w of the convective precipitation from Typhoon Matmo with the results from *Bringi et al.* [2003], it is found that the DSDs of convective precipitation in Matmo's rainband over land are close to the maritime convective type identified in *Bringi et al.* [2003]. Their study shows that the maritime (continental) type of convection has

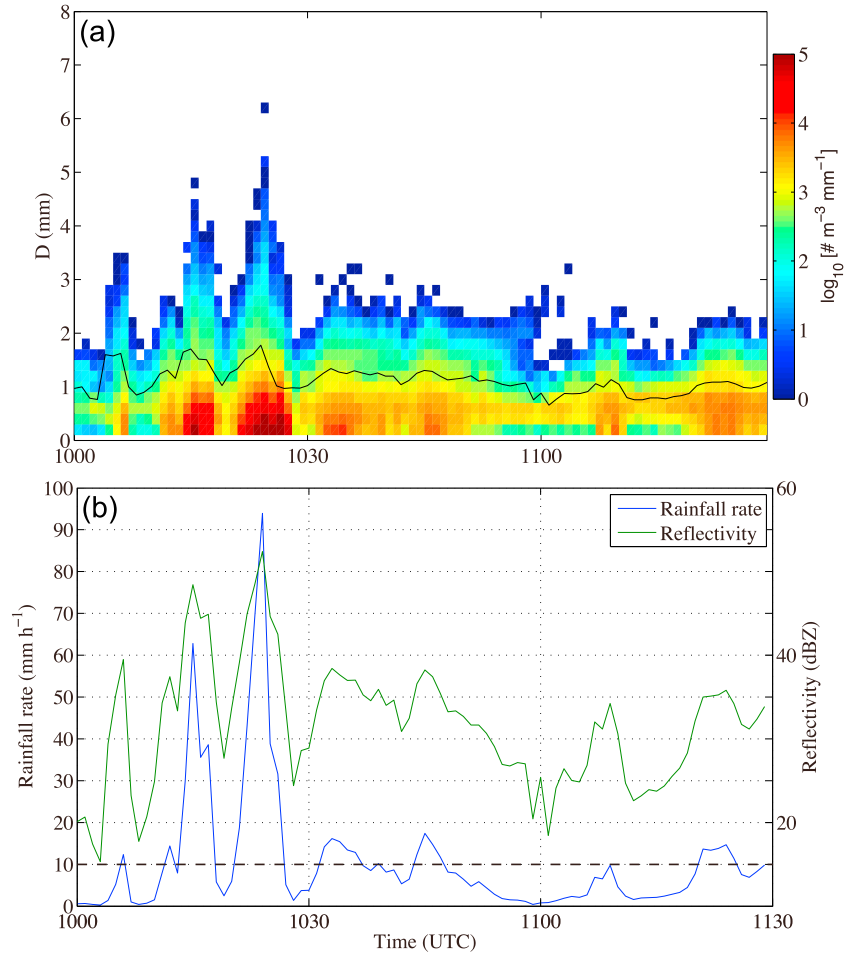

Figure 6. The time series of (a) the DSDs and (b) the rainfall rate (mm h^{-1}) and reflectivity (dB*Z*) calculated from the 2DVD during 1000–1130 UTC. The color shades represent the logarithmic number of particles in a particular size bin (mm^{-1}) within a unit volume (m^{-3}). The *y* axis in Figure 6a indicates the equivolume diameter (mm) of raindrops. The black line in Figure 6a represents the mass-weighted mean diameter D_m.

D_m ~ 1.5–1.75 mm (2–2.75 mm) and logarithmic N_w ~ 4–4.5 (3–3.5). In our case, the mean values of D_m and logarithmic N_w during the mature stage (Figure 7c) are 1.41 mm and 4.67, respectively. The distributions of D_m and N_w are only partially overlapped with the maritime region, suggesting that the DSDs of the rainband have a higher concentration of smaller raindrops than those in maritime convective precipitation and in typhoons making landfall in Taiwan (black dots in Figure 7) from *Chang et al*. [2009]. During the mature stage, the mean D_m is ~1.4 mm, 0.6 mm smaller than that in *Chang et al*. [2009]; the $\log_{10}(N_w)$ is ~0.9 higher than theirs, meaning that the number concentration is almost a magnitude higher than that of *Chang et al*. [2009]. The more humid environment and the significant topographic forcing over Taiwan might be the causes of the differences.

5. Vertical Structure of Kinematic and Microphysical Fields

The convective precipitation in the Matmo's rainband has a high rainfall rate and a DSD with a high concentration of small drops. Therefore, the following analyses are focused on the microphysical structures of the convective precipitation regions. An algorithm based on *Steiner et al*. [1995] is applied to reflectivity data at 2 km altitude in order to separate the convective and stratiform regions within Matmo's rainband. The same algorithm was also used to separate stratiform from convective precipitation over China in *Chen et al*. [2014].

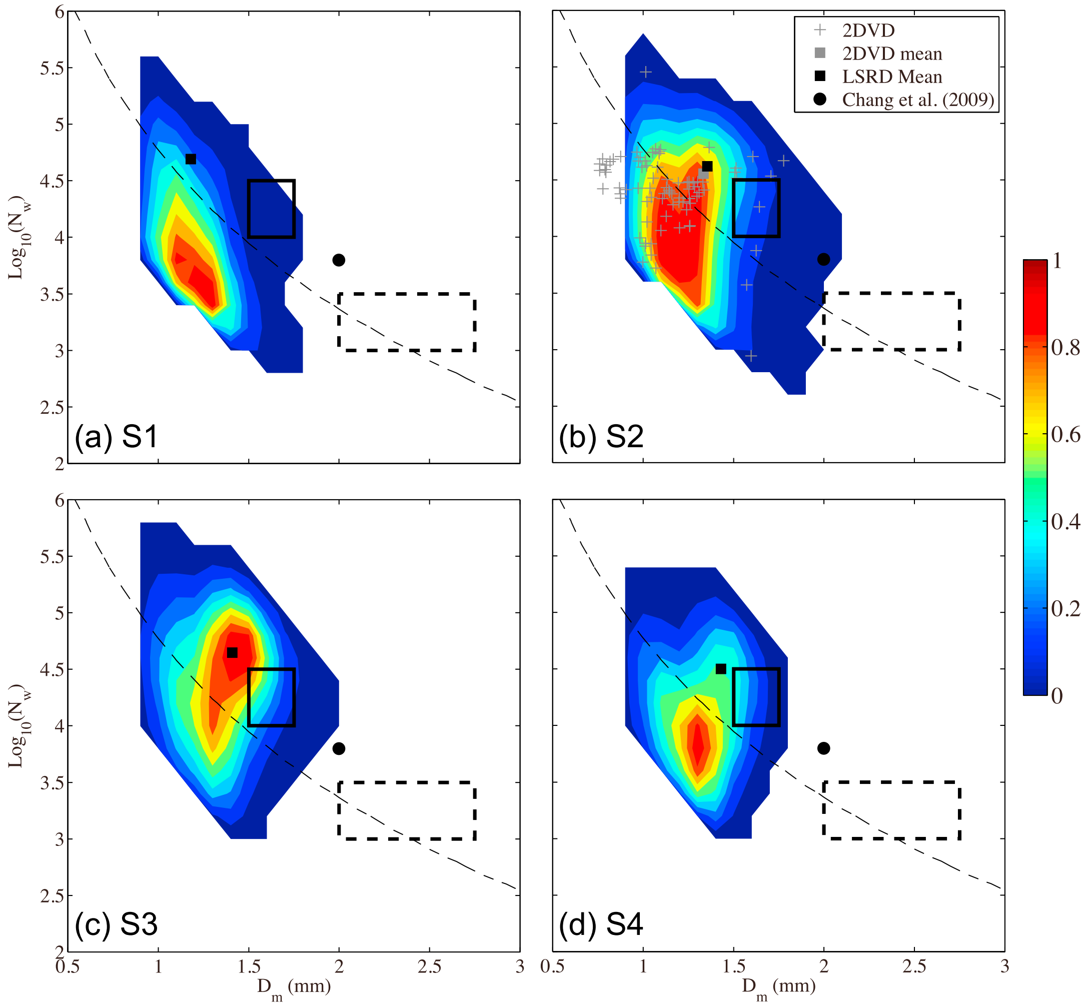

Figure 7. Frequency of occurrences (color shaded) of D_m (mm) and logarithmic N_w (mm^{-1} m^{-3}) of the retrieved DSDs from LSRD at four stages, (a) onset, (b) developing, (c) mature, and (d) dissipating. The gray crosses in Figure 7b represent the D_m and N_w values calculated from 2DVD. The dashed line indicates the rainfall rate of 10 mm h^{-1}. The two outlined squares represent (solid) the maritime and (dashed) continental types of convective systems. The gray square, black square, and black dot indicate the mean value of D_m and N_w from 2DVD, LSRD, and the study of *Chang et al.* [2009] for rainfall rate over 10 mm h^{-1}.

5.1. Composite Vertical Structure of Kinematic Fields

To examine the general features of the kinematic fields, the contoured frequency by altitude diagram (CFAD) [*Yuter and Houze*, 1995] is applied to the dual-Doppler analyses in the convective region. The CFADs of vertical velocity (w) and divergence of convection from S1, S2, and S3 are shown in Figure 8. Because of the limited dual-Doppler analysis domain, the CFAD of S4 is not included. Following *Hence and Houze* [2011], the bulk of the distribution contained within the contours for frequencies greater than 50% of the maximum frequency in the distribution (shading from red to yellow) is referred to as the modal distribution and the frequencies less than 50% as the outlier distribution.

As the rainband is intensifying, both updrafts and downdrafts are enhanced, exhibiting larger variance of w (Figures 8a–8c). The modal distribution of w is between −0.5 and 0.5 m s^{-1} below 3 km height, suggesting weak vertical motion in most of the convective region at low levels. During the mature stage, the updrafts over 5 m s^{-1} occurred at less than 5% of the peak frequency in the convective region (Figure 8c). The maximum updraft is ~9 m s^{-1}, consistent with a moderate CAPE (Figure 3). Similar to the vertical velocity, the convergence/divergence fields also show larger variances during mature stage (Figures 8e–8g). The modal distribution of convergence/divergence tilts from convergence (negative) to divergence (positive) as the altitude increases (Figures 8e–8g), indicating low-level convergence turning into high-level divergence at

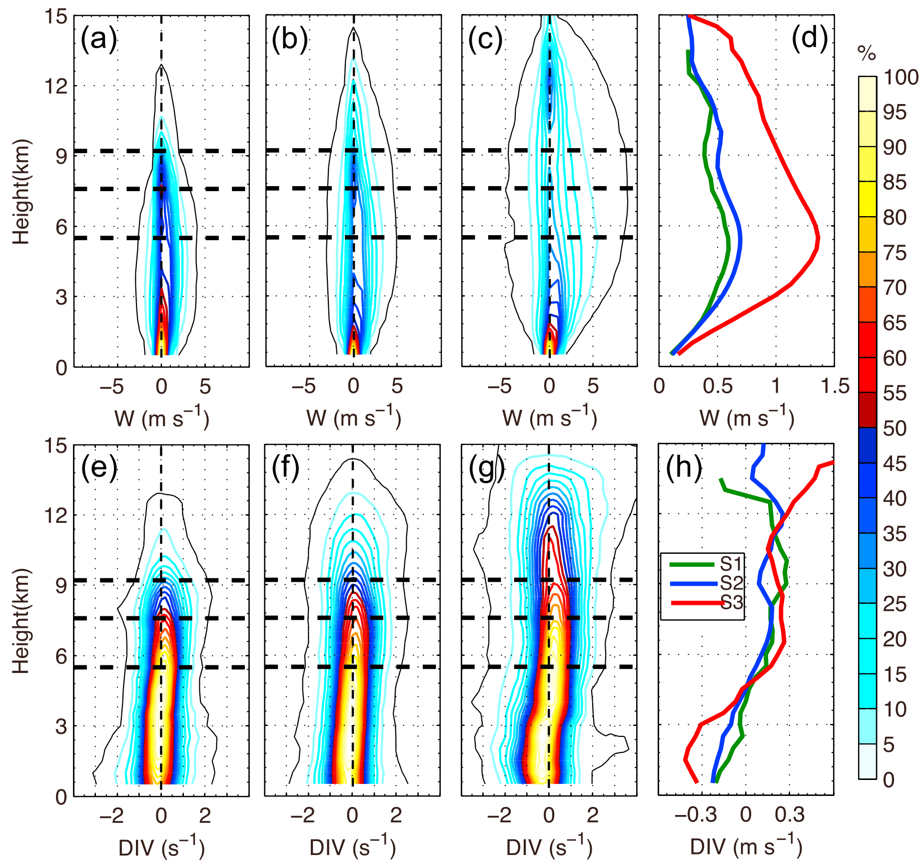

Figure 8. CFADs of the convective-only vertical velocity (W, m s^{-1}) during three stages, (a) onset (S1), (b) developing (S2), and (c) mature (S3). Contours represent the frequency of occurrence relative to the maximum absolute frequency in the data sample represented in the CFAD, contoured every 5%. The frequency over 50% is color shaded from red to yellow. The thick black dashed lines represent the level of 0°C, −10°C, and −20°C from bottom to top, respectively. (d) The averaged profiles of the convective-only vertical velocity from four stages. (e–h) Same as Figures 8a–8d, except for the divergence (s^{-1}).

~4.5 km altitude, which is favorable for and consistent with the presence of convection. The mean vertical profiles show intensifying low-level convergence and high-level divergence from S1 to S3 (Figure 8h), consistent with increasing vertical velocity (Figure 8d).

5.2. Composite Vertical Structure of Microphysical Fields

To investigate the vertical microphysical structures of the rainband, the CFADs of Z_H, Z_{DR}, and K_{DP} are presented in Figure 9, containing the normalized total accumulation CFADs for four different stages. During S1, the modal distribution of Z_H is between 25 and 40 dBZ, and the height of the model distribution of 35 dBZ is below freezing level (Figure 9a), meaning that the convection is moderate and mostly generated within warm clouds. The Z_{DR} during S1 are relatively small with the modal distribution between 0 and 0.8 dB (Figure 9f), and the values of K_{DP} are also quite small (Figure 9k), indicating limited water content. The increase in Z_H and Z_{DR} due to the melting of ice particles is evident near the freezing level during S1 (Figures 9a and 9f). Consistent with the increasing vertical velocity (Figure 8), the convection during S2 is stronger and deeper than that of S1 (Figure 9b). Due to the increasing vertical velocity, the raindrops have a longer time to grow larger, with the modal Z_{DR} being between 0.2 and 1.1 dB (Figure 9g) and the modal K_{DP} between 0.1 and 0.6 km^{-1} (Figure 9l). During the mature stage, the convection reaches peak height and intensity. The modal distribution of Z_H is between 35 and 50 dBZ, and the height of 35 dBZ reaches 7.5 km (Figure 9c). The raindrop size and water content also reach their maximum in terms of the modal distribution of Z_{DR} and K_{DP} (Figures 9h and 9m), and the K_{DP} maximum is close to 3°km^{-1}, indicating heavy rainfall. When the rainband is dissipating, the distributions of Z_H and Z_{DR} are quite similar to those at the mature stage

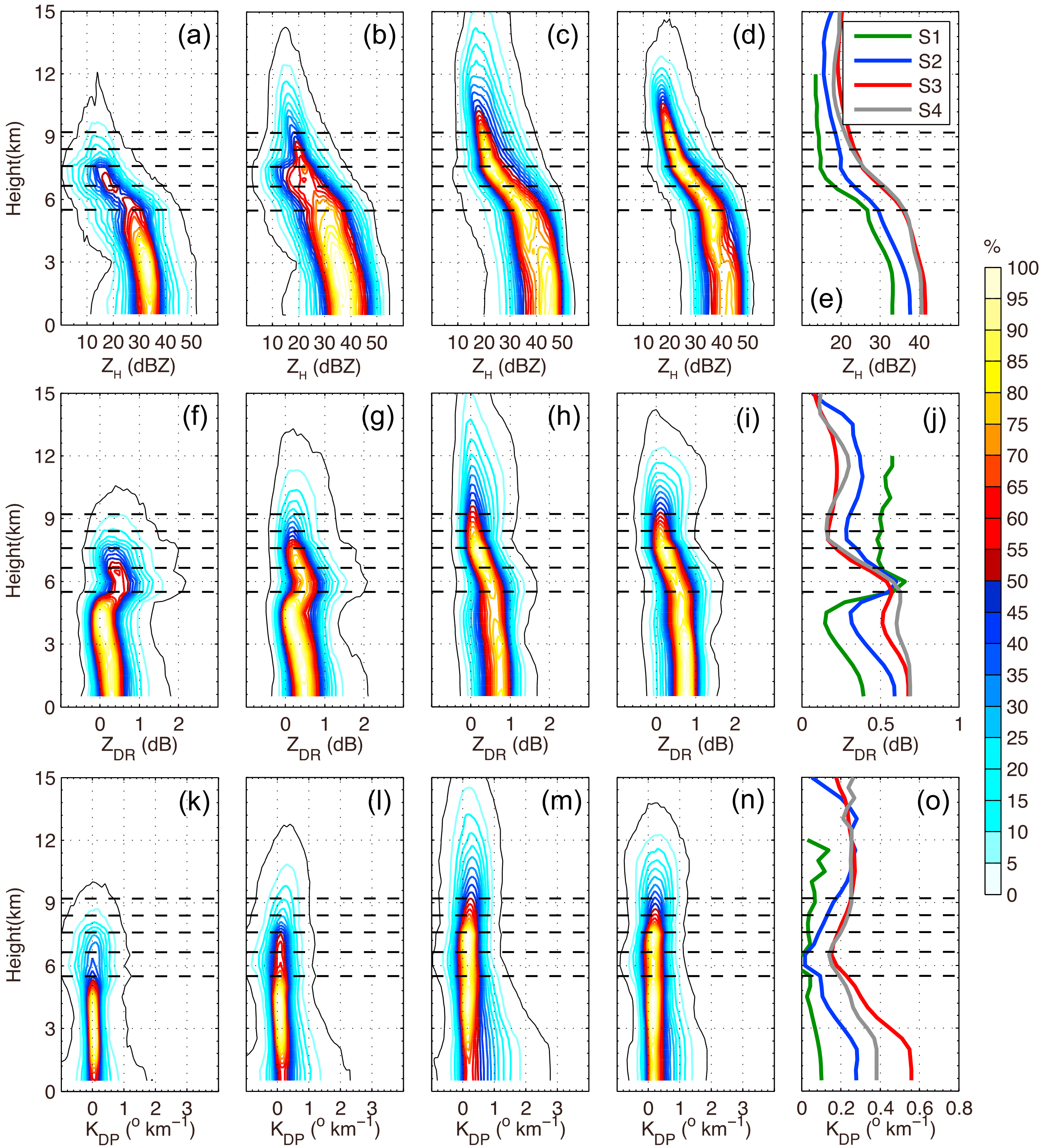

Figure 9. CFADs of the convective-only reflectivity data during four evolution stages, (a) onset (S1), (b) developing (S2), (c) mature (S3), and (d) dissipating (S4). Contours represent the frequency of occurrence relative to the maximum absolute frequency in the data sample represented in the CFAD, contoured every 5%. The frequency over 50% is color shaded. The thick black dashed lines represent the level of 0°C, −5°C, −10°C, −15°C, and −20°C from bottom to top, respectively. (e) The averaged profiles of the convective-only reflectivity from four stages. (f–j) Same as Figures 9a–9e but for Z_{DR}. (k–o) Same as Figures 9a–9e but for K_{DP}.

(Figures 9d and 9i). However, K_{DP} is clearly decreased in terms of both modal and outlier distributions (Figure 9n), which means that the number concentration has been reduced.

5.3. Important Microphysical Processes

The vertical mean profiles of Z_H (Figure 9e), Z_{DR} (Figure 9j), and K_{DP} (Figure 9o) are further calculated to examine the evolution of the vertical microphysical structures. Given by the relatively dry environment above the −20°C level (Figure 3), the ice crystals tend to grow slowly during S1 due to limited ice supersaturation [*Bailey and Hallett*, 2009], and the ice particles tend to have higher density and regular shapes (more like single crystal with larger axis ratio than raindrops), resulting in a large Z_{DR}. Z_H and K_{DP} during S1 are considerably smaller than S2 and S3, suggesting that the ice crystals have a smaller number concentration. According to the sounding in Figure 3, the environment is moist at lower levels and dry at upper levels. The water vapor can be transported from lower levels into the higher levels by the updrafts. As the updrafts are intensifying, more water vapor is transported to the upper levels, which leads to distinct ice supersaturation above −20°C level. Thus, the ice crystals would grow faster with more irregular shape and larger size [*Bailey and Hallett*, 2009] and lower density [*Heymsfield et al*., 2004], which generally makes the Z_{DR} decreasing. The increasing ice particle size, number concentration, and ice water content corresponding to the fast growth lead to increasing Z_H and K_{DP}.

Between ~ 9 km and ~7 km, Z_H and Z_{DR} substantially increase and K_{DP} decreases with decreasing altitudes during S2, S3, and S4 (Figures 9e, 9j, and 9o). In this layer, deposition, aggregation, riming, and even secondary ice production can affect the ice growth, although the dominant mechanism cannot be identified. According to the decreasing K_{DP}, the aggregation process should play an important role in this layer [*Andrić et al*., 2012]. Below −5°C to the freezing level, the signature of melting is clear, with Z_H, Z_{DR}, and K_{DP} increasing with decreasing altitudes (Figures 9e, 9j, and 9o). It is noticed that the melting signature is higher than the freezing level (ambient 0°C level from sounding). This can be due to the higher temperature of the lifted air parcels than the ambient temperature [*Shusse et al*., 2010] because of the latent heat release from water vapor condensation, which is also evident in Figure 3. Above the freezing level, the Z_{DR} is generally smaller during S3 and S4 than S1 and S2 (Figure 9j), suggesting that the ice particles tend to be more spherical or have lower density. The corresponding K_{DP} would be also smaller during S3 and S4 than S1 and S2 if the number concentration is the same [*Bringi and Chandrasekar*, 2001]. Thus, the larger K_{DP} above freezing level during S3 and S4 than S1 and S2 implies a higher number concentration of ice particles compared to S1 and S2 (Figure 9o).

Below the freezing level, the Z_H, Z_{DR}, and K_{DP} increase downward to ~ 2 km and then remain constant to the ground (Figures 9e, 9j, and 9o). These signatures indicate the processes of collision coalescence and/or the accretion of cloud water by raindrops [*Rosenfeld and Ulbrich*, 2003; *Kumjian and Prat*, 2014]. The near constant Z_H, Z_{DR}, and K_{DP} below 2 km may be an artifact of the limited coverage by the lowest elevation of LSLD. As the rainband intensifies with increasing vertical motion, the raindrops would have longer time for coalescence and accretion of cloud water before they can overcome the updraft and fall to the ground, which is consistent with the quantitative DSD analyses (Figure 7). The downward increase of K_{DP} becomes larger (smaller), suggesting more (less) precipitation water content as the rainband intensifies (dissipates).

6. The Dominant Microphysical Processes and Precipitation Efficiency

6.1. Dominant Microphysical Processes

The aforementioned analyses show that both ice and warm rain processes can play important roles in the rainband precipitation. To separate the contributions of ice and warm rain processes to surface precipitation, liquid and ice water content estimation (see equations in section 2.3.2) is applied to the LSRD observations. The liquid and ice water contents estimated for the four stages are shown in Figure 10. The ice water content increases as the rainband intensifies, due to the enhanced ice processes corresponding to the increased vertical motion. In contrast, the ice water content decreases as the rainband dissipates with decreased vertical motion. The maximum ice water content is ~ 0.24 g m^{-3} in the mature stage. However, the liquid water content is an order of magnitude larger than the ice water content during each of the four stages. The maximum liquid water content is ~ 2.5 g m^{-3} in the mature stage. Even if the ice water above freezing level were to be completely melted into liquid water, it would account only for about 10% of the liquid water below freezing level. This suggests that the warm rain processes are dominant in the heavy rainfall produced in Matmo's rainband.

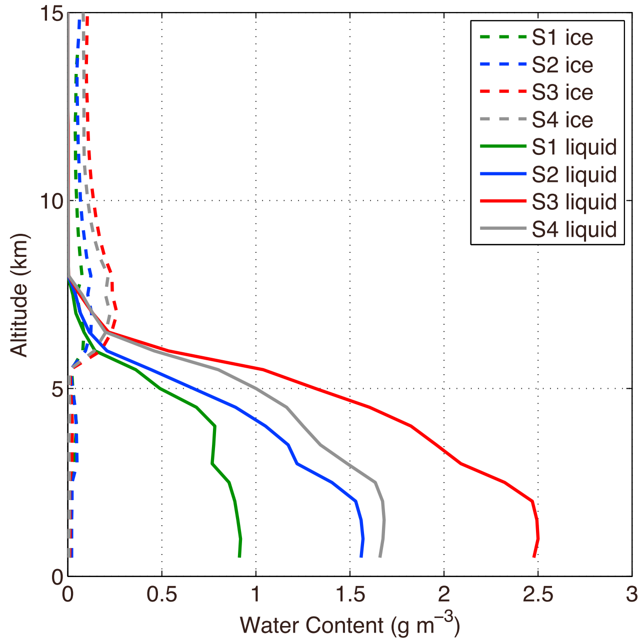

Figure 10. Mean values of ice (dashed) and liquid (solid) water content (g m^{-3}) in the convective region using Z_{DP}-Z^{rain} relation at four different stages.

The liquid water content increases rapidly from the freezing level down to about 2 km height (Figure 10). The collision-coalescence processes lead to increasing Z_H, Z_{DR}, and K_{DP}; however, they do not change the water content detected by the radar [*Kumjian and Prat*, 2014]. Also, the DSD shifts to larger diameters from 5 km to 2 km height (Figure 11), indicating the increase of drop size through accretion of cloud particles [*Rosenfeld and Ulbrich*, 2003]. The growth rate of raindrops from 5 km to 2 km height slightly increases as a function of the raindrop size. In other word, the larger raindrops have slightly larger growth rate (Figure 11) than the smaller raindrops, which can be attributed to the larger accretion rate [*Rosenfeld and Ulbrich*, 2003]. Thus, the rapid growth of the liquid water content mainly comes from the conversion of cloud water into rainwater via accretion of cloud water by raindrops. The very moist environment and the low cloud base (Figure 3) ensure that this accretion process occurs over a large depth.

6.2. Precipitation Efficiency

Previous studies have shown that warm rain accretion in deep warm clouds tends to produce high precipitation efficiency (PE) and causes heavy rainfall [*Rowe et al.*, 2008; *Murata*, 2009]. *Murata* [2009] found that the conversion of cloud water to rainwater via accretion dominated the heavy precipitation and produced very high rainfall efficiencies of 50%–60% in numerical simulations of Typhoon Meari (2004). The PE of Typhoon Matmo (2014) is examined here.

The PE is defined as the ratio between total rainfall (R_{tot}) to the total water vapor (Q_{tot}) supply of a precipitation system:

$$\mathrm{PE} = \frac{R_{tot}}{Q_{tot}} \times 100\%. \tag{10}$$

The calculation of PE follows the procedure in *Chang et al.* [2015], which requires the information of the kinematic, moisture, and rainfall rate [*Chang et al.*, 2015, equations (7) and (8)]. The bottom boundary for the calculation is chosen at 2 km altitude to have better spatial coverage of the LSRD observations. The rainfall rate is estimated at the 2 km altitude from the LSRD measurements. An algorithm combining the K_{DP}-R and Z-R relations from LSRD is used in this study [*Cifelli et al.*, 2002; *Chang et al.*, 2015] as follows:

$$R = 64.06 K_{DP}^{0.78} \left(\mathrm{mm\ h^{-1}}\right) \ \text{when}\ Z_{HH} > 30\ \mathrm{dB}\ \text{and}\ K_{DP} > 0.5^\circ\ \mathrm{km^{-1}}; \tag{11}$$

otherwise, the Z-R relation is used,

$$R = \left(\frac{Z_{HH}}{160.37}\right)^{1/1.37} \left(\mathrm{mm\ h^{-1}}\right). \tag{12}$$

The coefficients of (11) and (12) are obtained from the 2DVD data.

The kinematic fields, vertical velocity and divergence, are determined by the dual-Doppler wind analyses. The impact of the vertical velocity uncertainty within the dual-Doppler analyses on the PE calculation is also

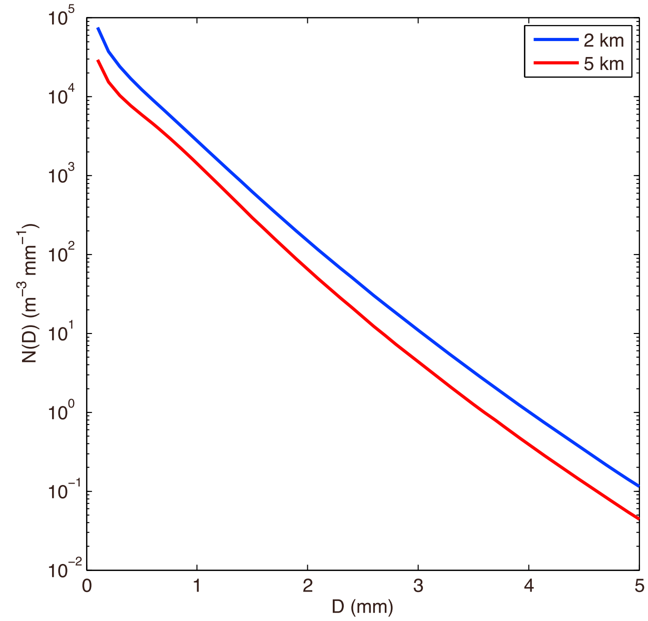

Figure 11. The composite drop size distribution within the convective area at 2 km and 5 km at 1202 UTC 24 July 2014.

considered. According to *Doviak et al.* [1976], the standard deviation of the vertical velocity is ~2.0 m s^{-1} for upward integration at 2 km height. Although the variational integration scheme is used in this study, the standard deviation of 2 m s^{-1} can be representative to the accuracy of the vertical velocity at 2 km height. To take the uncertainty into account, 100 members of vertical velocities are generated by adding Gaussian random perturbations with zero mean and 2 m s^{-1} standard deviation to the vertical velocity at 2 km, and then, 100 PEs and their mean are calculated. The moisture fields of the ambient environment are provided by the

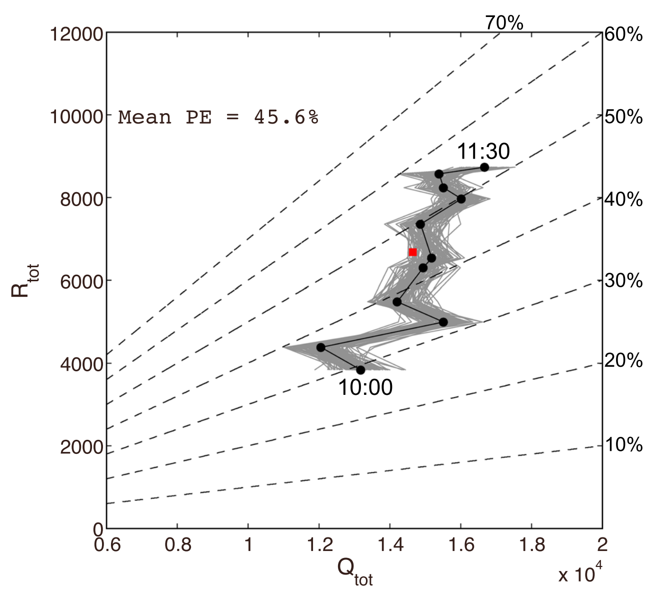

Figure 12. The 100 members (gray lines) and their mean (black solid line with dots) of total rainfall flux (R_{tot}, kg km^{-2} s^{-1}) and total water vapor flux (Q_{tot}, kg km^{-2} s^{-1}) from cloud base (2.0 km) of available dual-Doppler analyses of convective precipitation regions during 1000 UTC to 1130 UTC (developing stage) every 8 min. The red square represents the mean values of R_{tot} and Q_{tot}. The dashed lines represent precipitation efficiency from 10% to 70%.

sounding data at JN (Figure 1). The same as in *Chang et al.* [2015], R_{tot} and Q_{tot}, in units of kg km^{-2} s^{-1}, are normalized by the system size and integration time window.

The calculated 100 members and their mean of R_{tot} and Q_{tot} in convective precipitation regions during developing stage (1000 UTC–1130 UTC) are shown in Figure 12. The PE members have similar tendencies with spreads less than 5%. The mean instantaneous PEs (the ratio between R_{tot} and Q_{tot}) generally increase from about 30% to 60% as the rainband intensifies, which is consistent with the accelerated accretion process. R_{tot}, Q_{tot}, and PE are further averaged over the developing stage (1.5 h). Overall, the mean PE is about 46% during the developing stage, while the PEs are over 50% after 1100 UTC. The PE during the mature stage is expected to be higher than the developing stage; however, it is not calculated because the rainband is only partially covered by the dual-Doppler analysis domain. The PE in this study is close to the PE (50–60%) calculated from a precipitation event associated with typhoon near southern Japan based on numerical simulation data in *Murata* [2009]. The conversion of cloud water into rainwater through the accretion of cloud water is emphasized to be an important mechanism attributing to the enhancement of PE, and the environment with high moisture provides deep layer of warm cloud which is favorable for the accretion process.

7. Summary and Conclusions

In 2014, landfalling Typhoon Matmo (2014) moved inland and passed over an observation area of OPACC field campaign in near Nanjing in eastern China. The convection north of Matmo's center was organized into a rainband from 0800 to 1500 UTC of 24 July. It was well captured by a research S band polarimetric Doppler radar (LSRD) located in Lishui, an operational single-polarization S band Doppler radar (NJRD), and a third-generation two-dimensional video disdrometer (2DVD) located in Nanjing. Based on these unique (in mainland China) observations, this study explored the detailed kinematic and microphysical structures and the corresponding microphysical processes of a TC rainband throughout its life cycle after the TC landfall.

The rainband developed in an environment characterized by high relative humidity (over 80% below 400 hPa), high freezing level (~5.5 km), and moderate CAPE (~1400 J kg^{-1} with positive areas uniformly distributed between 900 and 150 hPa), favorable for the warm rain processes. Under such environmental conditions, the rainfall of the Matmo rainband is characterized as having high concentrations of small/medium size drops based on the 2DVD-measured and LSRD-retrieved DSDs. The mean values of mean mass diameter D_m and logarithmic normalized intercept N_w of convective precipitation during the mature stage are 1.41 mm and 4.67 $\log_{10}$ mm^{-1} m^{-3}, respectively, indicating that the DSDs of the rainband have even smaller raindrops and higher concentrations compared to maritime convective precipitation as studied by *Bringi et al.* [2003].

The general vertical structures of kinematic and microphysical fields are illustrated using CFADs. The low-level convergences (upper level divergences) and updrafts are enhanced as the rainband intensifies, which is consistent with the intensifying convection. Consistent with the kinematic structure, the microphysical fields reveal corresponding enhancement of convection, as evidenced by the increased rainfall rate and water content. The estimated vertical profiles of ice and liquid water contents show that the water content growth is achieved mainly through warm rain processes, primarily from the conversion of cloud water to rainwater through cloud water accretion by the raindrops. Based on the kinematic fields retrieved from dual-Doppler wind analysis, the moisture fields from sounding data, and the rainfall rate estimated from polarimetric variables, the precipitation efficiency (PE) for the rainband during the developing stage is evaluated. The mean PE is about 46% during the developing stage, and the instantaneous PEs are generally over 50% after 1100 UTC, indicating that the accretion of cloud water is an important mechanism in producing heavy rainfall, consistent with previous results based on numerical simulations.

Although the warm rain process dominates the heavy rainfall, the ice particles may still play an important role as seeders and accelerate the accretion process. The ice particles are generated above the 0°C level and grow to produce snow aggregates, graupels, etc. The heavier particles melt into raindrops and then could collect the cloud water by accretion to obtain more liquid water before they reach the ground. When the rainband intensifies, the ice particles would have larger mass (either larger size or higher density) to overcome the intensified updraft. The raindrop populations directly below the freezing level during the mature stage with larger sizes and higher number concentrations relative to other stages are evident from enhanced Z_{DR} and K_{DP}. These drop populations directly below the freezing level, which may result from the melting process described above, can enhance the water content growth by accelerating the accretion process because the accretion efficiency is proportional to the size and number concentration of raindrops [*Brandes et al*., 2006]. In general, the conversion of cloud water into rainwater through cloud water accretion by raindrops dominates the heavy rainfall, while the ice particles generated by the ice processes may also play a role in accelerating the accretion process.

The DSDs of the rainband in this study are quite different from those TC rainbands observed in other basins or even the typhoons making landfall over the Taiwan. The physical/microphysical processes resulting in such differences are worthy of further studies through more observational studies and/or high-resolution numerical simulations.

Acknowledgments
This work was primarily supported by the National Fundamental Research 973 Program of China (2013CB430101 and 2015CB452801) and the National Natural Science Foundation of China (grants 41605026, 41275031, 41322032, and 41475015). We would also like to acknowledge the China Meteorological Administration and PLA University of Science and Technology for collecting and archiving the radar data used in this study. Data used in this work are from the National Fundamental Research 973 Program of China (2013CB430101). According to the data policy of this program and China Meteorological Administration, the data used to produce the results of this paper can be accessed publicly after 2018 at http://scw973.nju.edu.cn/outside.asp.

References

Andrić, J., M. R. Kumjian, D. S. Zrnić, J. M. Straka, and V. M. Melnikov (2012), Polarimetric signatures above the melting layer in winter storms: An observational and modeling study, *J. Appl. Meteorol. Climatol.*, *52*(3), 682–700, doi:10.1175/JAMC-D-12-028.1.

Bailey, M. P., and J. Hallett (2009), A comprehensive habit diagram for atmospheric ice crystals: Confirmation from the laboratory, AIRS II, and other field studies, *J. Atmos. Sci.*, *66*(9), 2888–2899, doi:10.1175/2009JAS2883.1.

Brandes, E. A., G. Zhang, and J. Sun (2006), On the influence of assumed drop size distribution form on radar-retrieved thunderstorm microphysics, *J. Appl. Meteorol. Climatol.*, *45*(2), 259–268, doi:10.1175/JAM2335.1.

Bringi, V. N., and V. Chandrasekar (2001), *Polarimetric Doppler Weather Radar: Principles and Applications*, Cambridge Univ. Press, New York.

Bringi, V. N., V. Chandrasekar, J. Hubbert, E. Gorgucci, W. L. Randeu, and M. Schoenhuber (2003), Raindrop size distribution in different climatic regimes from disdrometer and dual-polarized radar analysis, *J. Atmos. Sci.*, *60*(2), 354–365, doi:10.1175/1520-0469(2003)060<0354:RSDIDC>2.0.CO;2.

Brown, B. R., M. M. Bell, and A. J. Frambach (2016), Validation of simulated hurricane drop size distributions using polarimetric radar, *Geophys. Res. Lett.*, *43*, 910–917, doi:10.1002/2015GL067278.

Cao, Q., G. Zhang, E. Brandes, T. Schuur, A. Ryzhkov, and K. Ikeda (2008), Analysis of video disdrometer and polarimetric radar data to characterize rain microphysics in Oklahoma, *J. Appl. Meteorol. Climatol.*, *47*(8), 2238–2255, doi:10.1175/2008JAMC1732.1.

Carey, L. D., and S. A. Rutledge (2000), The relationship between precipitation and lightning in tropical island convection: A C-band polarimetric radar study, *Mon. Weather Rev.*, *128*(8), 2687–2710, doi:10.1175/1520-0493(2000)128<2687:TRBPAL>2.0.CO;2.

Chang, W.-Y., T.-C. C. Wang, and P.-L. Lin (2009), Characteristics of the raindrop size distribution and drop shape relation in typhoon systems in the Western Pacific from the 2D video disdrometer and NCU C-band polarimetric radar, *J. Atmos. Oceanic Technol.*, *26*(10), 1973–1993, doi:10.1175/2009JTECHA1236.1.

Chang, W.-Y., W.-C. Lee, and Y.-C. Liou (2015), The kinematic and microphysical characteristics and associated precipitation efficiency of subtropical convection during SoWMEX/TiMREX, *Mon. Weather Rev.*, *143*(1), 317–340, doi:10.1175/MWR-D-14-00081.1.

Chen, B., Y. Wang, and J. Ming (2012), Microphysical characteristics of the raindrop size distribution in Typhoon Morakot (2009), *J. Trop. Meteorol.*, *18*(02), 162–171.

Chen, X., K. Zhao, and M. Xue (2014), Spatial and temporal characteristics of warm season convection over Pearl River Delta region, China, based on 3 years of operational radar data, *J. Geophys. Res. Atmos.*, *119*, 12,447–12,465, doi:10.1002/2014JD021965.

Cifelli, R., W. A. Petersen, L. D. Carey, S. A. Rutledge, and M. A. F. da Silva Dias (2002), Radar observations of the kinematic, microphysical, and precipitation characteristics of two MCSs in TRMM LBA, *J. Geophys. Res.*, *107*(D20), 8077, doi:10.1029/2000JD000264.

Crum, T. D., R. L. Alberty, and D. W. Burgess (1993), Recording, archiving, and using WSR-88D data, *Bull. Am. Meteorol. Soc.*, *74*(4), 645–653, doi:10.1175/1520-0477(1993)074<0645:RAAUWD>2.0.CO;2.

Didlake, A. C., and R. A. Houze (2009), Convective-scale downdrafts in the principal rainband of hurricane Katrina (2005), *Mon. Weather Rev.*, *137*(10), 3269–3293, doi:10.1175/2009MWR2827.1.

Doviak, R. J., and D. S. Zrnić (2006), *Doppler Radar and Weather Observations*, 2nd ed., Dover, New York.

Doviak, R. J., P. S. Ray, R. G. Strauch, and L. J. Miller (1976), Error estimation in wind fields derived from dual-doppler radar measurement, *J. Appl. Meteorol.*, *15*(8), 868–878, doi:10.1175/1520-0450(1976)015<0868:EEIWFD>2.0.CO;2.

Duan, Y., and J. Liu (2010), TC precipitation (QPE/QPF) and related inland flood modeling, La Réunion, France.

Giangrande, S. E., and A. V. Ryzhkov (2008), Estimation of rainfall based on the results of polarimetric echo classification, *J. Appl. Meteorol. Climatol.*, *47*(9), 2445–2462, doi:10.1175/2008JAMC1753.1.

Hence, D. A., and R. A. Houze (2011), Vertical structure of hurricane eyewalls as seen by the TRMM precipitation radar, *J. Atmos. Sci.*, *68*(8), 1637–1652, doi:10.1175/2011JAS3578.1.

Hence, D. A., and R. A. Houze (2012), Vertical structure of tropical cyclone rainbands as seen by the TRMM precipitation radar, *J. Atmos. Sci.*, *69*(9), 2644–2661, doi:10.1175/JAS-D-11-0323.1.

Heymsfield, A. J., A. Bansemer, C. Schmitt, C. Twohy, and M. R. Poellot (2004), Effective ice particle densities derived from aircraft data, *J. Atmos. Sci.*, *61*(9), 982–1003, doi:10.1175/1520-0469(2004)061<0982:EIPDDF>2.0.CO;2.

Kumjian, M. R. (2013), Principles and applications of dual-polarization weather radar. Part I: Description of the polarimetric radar variables, *J. Oper. Meteorol.*, *1*(19), 226–242.

Kumjian, M. R., and O. P. Prat (2014), The impact of raindrop collisional processes on the polarimetric radar variables, *J. Atmos. Sci.*, *71*(8), 3052–3067, doi:10.1175/JAS-D-13-0357.1.

Kumjian, M. R., and A. V. Ryzhkov (2012), The impact of size sorting on the polarimetric radar variables, *J. Atmos. Sci.*, *69*(6), 2042–2060, doi:10.1175/JAS-D-11-0125.1.

May, P. T., J. D. Kepert, and T. D. Keenan (2008), Polarimetric radar observations of the persistently asymmetric structure of tropical cyclone ingrid, *Mon. Weather Rev.*, *136*(2), 616–630, doi:10.1175/2007MWR2077.1.

Mohr, C. G., L. Jay Miller, R. L. Vaughan, and H. W. Frank (1986), The merger of mesoscale datasets into a common Cartesian format for efficient and systematic analyses, *J. Atmos. Oceanic Technol.*, *3*(1), 143–161, doi:10.1175/1520-0426(1986)003<0143:TMOMDI>2.0.CO;2.

Morrison, H., G. Thompson, and V. Tatarskii (2009), Impact of cloud microphysics on the development of trailing stratiform precipitation in a simulated squall line: Comparison of one- and two-moment schemes, *Mon. Weather Rev.*, *137*(3), 991–1007, doi:10.1175/2008MWR2556.1.

Murata, A. (2009), A mechanism for heavy precipitation over the Kii Peninsula accompanying Typhoon Meari (2004), *J. Meteorol. Soc. Jpn. Ser. II*, *87*(1), 101–117, doi:10.2151/jmsj.87.101.

Rosenfeld, D., and C. W. Ulbrich (2003), Cloud microphysical properties, processes, and rainfall estimation opportunities, *Meteorol. Monogr.*, *30*(52), 237–258, doi:10.1175/0065-9401(2003)030<0237:CMPPAR>2.0.CO;2.

Rowe, A. K., S. A. Rutledge, T. J. Lang, P. E. Ciesielski, and S. M. Saleeby (2008), Elevation-dependent trends in precipitation observed during NAME, *Mon. Weather Rev.*, *136*(12), 4962–4979, doi:10.1175/2008MWR2397.1.

Schuur, T., A. Ryzhkov, P. Heinselman, D. Zrnic, D. Burgess, and K. Scharfenberg (2003), Observations and classification of echoes with the polarimetric WSR-88D radar, NOAA/Natl. Severe Storms Lab. Rep.

Shusse, Y., N. Takahashi, K. Nakagawa, S. Satoh, and T. Iguchi (2010), Polarimetric radar observation of the melting layer in a convective rainfall system during the rainy season over the East China Sea, *J. Appl. Meteorol. Climatol.*, *50*(2), 354–367, doi:10.1175/2010JAMC2469.1.

Steiner, M., R. A. Houze, and S. E. Yuter (1995), Climatological characterization of three-dimensional storm structure from operational radar and rain gauge data, *J. Appl. Meteorol.*, *34*(9), 1978–2007, doi:10.1175/1520-0450(1995)034<1978:CCOTDS>2.0.CO;2.

Testud, J., S. Oury, R. A. Black, P. Amayenc, and X. Dou (2001), The concept of "normalized" distribution to describe raindrop spectra: A tool for cloud physics and cloud remote sensing, *J. Appl. Meteorol.*, *40*(6), 1118–1140, doi:10.1175/1520-0450(2001)040<1118:TCONDT>2.0.CO;2.

Tokay, A., P. G. Bashor, E. Habib, and T. Kasparis (2008), Raindrop size distribution measurements in tropical cyclones, *Mon. Weather Rev.*, *136*(5), 1669–1685, doi:10.1175/2007MWR2122.1.

Ulbrich, C. W. (1983), Natural variations in the analytical form of the raindrop size distribution, *J. Climate Appl. Meteorol.*, *22*(10), 1764–1775, doi:10.1175/1520-0450(1983)022<1764:NVITAF>2.0.CO;2.

Ulbrich, C. W., and L. G. Lee (2002), Rainfall characteristics associated with the remnants of tropical storm Helene in upstate South Carolina, *Weather Forecast.*, *17*(6), 1257–1267, doi:10.1175/1520-0434(2002)017<1257:RCAWTR>2.0.CO;2.

Vivekanandan, J., G. Zhang, and E. Brandes (2004), Polarimetric radar estimators based on a constrained gamma drop size distribution model, *J. Appl. Meteorol.*, *43*(2), 217–230, doi:10.1175/1520-0450(2004)043<0217:PREBOA>2.0.CO;2.

Wilson, J. W., and D. M. Pollock (1974), Rainfall measurements during hurricane Agnes by three overlapping radars, *J. Appl. Meteorol.*, *13*(8), 835–844, doi:10.1175/1520-0450(1974)013<0835:RMDHAB>2.0.CO;2.

Yuter, S. E., and R. A. Houze Jr. (1995), Three-dimensional kinematic and microphysical evolution of Florida cumulonimbus. Part I: Spatial distribution of updrafts, downdrafts, and precipitation, *Mon. Weather Rev.*, *123*(7), 1921–1940, doi:10.1175/1520-0493(1995)123<1921:TDKAME>2.0.CO;2.

Zhang, G., J. Vivekanandan, and E. Brandes (2001), A method for estimating rain rate and drop size distribution from polarimetric radar measurements, *IEEE Trans. Geosci. Remote Sens.*, *39*(4), 830–841, doi:10.1109/36.917906.